

# WHITE DWARF MERGERS IN SMOOTHED-PARTICLE AND MOVING MESH HYDRODYNAMICS

CHENCHONG ZHU, RÜDIGER PAKMOR, PHILIP CHANG, MARTEN H. VAN KERKWIJK

(Dated: June 15, 2016)

*Draft version June 15, 2016*

## ABSTRACT

White dwarf binary mergers, the possible progenitors to a number of unusual stars and transient phenomena, can currently only be directly studied in detail through hydrodynamic simulations. These simulations have almost completely been performed using smoothed-particle hydrodynamics, a scheme known to produce numerical artifacts under certain conditions. In order to determine if there is a code dependence for mergers, we simulated the merging of a  $0.625 - 0.65 M_{\odot}$  carbon-oxygen white dwarf binary in both GASOLINE SPH and AREPO, which performs hydrodynamics on a moving mesh. We find that, just following the coalescence of the two white dwarfs, the AREPO merger remnant shows greater disturbance in the  $0.65 M_{\odot}$  accretor, as well as a greater temperature contrast between the dense, degenerate core of the remnant and the hot envelope surrounding it. Following the coalescence of the two stars, the GASOLINE simulation rapidly achieves axisymmetry and maintains the merger remnant as an oblate, rotationally supported object, while the AREPO remnant core stays asymmetric, and launches spiral waves into its surroundings that transport angular momentum at a rate comparable to that of the standard  $\alpha$ -viscosity formulation. These code-dependent differences in merger simulations could substantially affect processes immediately following the merger, from magnetic field dynamo processes to the possible onset of a nuclear detonation. The final product, of the merging process, however, likely remains a spherically symmetric dense core surrounded by a hot, non-degenerate envelope, regardless of which code is used.

**Key words:** binaries: close – white dwarfs – hydrodynamics – supernovae: general

## 1. INTRODUCTION

Simulations of WD mergers are a window into the detailed dynamics of the merging process and – since mergers cannot directly be seen using current observational capabilities – a link between observations of strange stars and explosive transients and theories about their formation. Since the pioneering work of Benz et al. (1990), these simulations have overwhelmingly used a single numerical hydrodynamics implementation, smoothed-particle hydrodynamics (SPH; eg. Monaghan 2005; Springel 2010b), to model WD mergers. SPH represents a fluid with a set of particles. The fluid’s continuum properties can be determined by using these particles as interpolation points, while the fluid’s evolution is determined by tracking the particles’ motions over time. SPH’s Lagrangian nature means regions of high density are automatically more resolved and advection is simulated without errors, and its equations of motion also inherently conserve energy, linear and angular momentum. These features make it much easier to model the bulk fluid motion, large density contrasts and complicated geometry of mergers in SPH than in Eulerian grid schemes<sup>1</sup>, which have difficulty simulating mergers except under specific coordinate systems and symmetries (see Katz et al. (2016) for recent developments). Building on Benz et al. and other early works such as Segretain et al. (1997) and Guerrero et al. (2004), more recent efforts has focused on more precise binary initial conditions (Dan et al. 2011), exploration of remnant properties across parameter space (Lorén-Aguilar et al. 2009; Raskin et al. 2012; Zhu et al. 2013; Dan et al. 2014) and exploring the possible instigation and consequences of a thermodynamic transient caused by the merger (eg. Pakmor et al. 2010; Dan et al. 2012; Pak-

mor et al. 2013; Moll et al. 2014; Raskin et al. 2014).

The standard SPH formulation is not without its problems, however. In order to provide enough dissipation to properly treat shocks, SPH uses an artificial viscosity, which can produce spurious heating and angular momentum transport in shear flows. While a number of standard remedies exist (eg. Springel 2010b Sec. 2.3), two of which we use in this work, their effectiveness in systems where shearing and shocks occur in close proximity is questionable. Errors in SPH interpolation produce noise on the scale of the interpolating kernel smoothing length, which can smear out shocks and steep gradients (Springel 2010b). Classical formulations of SPH have also been known to suppress hydrodynamic instabilities (eg. Agertz et al. 2007), and while this has subsequently been resolved by better treatments of contact discontinuities (eg. (Hopkins 2013; Hu et al. 2014; Keller et al. 2014)), the vast majority of SPH simulations in the literature do not include them. Shocks, large-scale shear flows and the formation of instabilities are all expected for WD mergers, and past comparisons between SPH and Eulerian grid codes for a diversity of astrophysical phenomena (eg. de Val-Borro et al. 2006; Trac et al. 2007; Mitchell et al. 2009) have often shown qualitative and resolution-independent differences.

A recent alternative to SPH, as well as Eulerian grid codes, is AREPO (Springel 2010a), one of a growing class of hydrodynamics codes (eg. Duffell & MacFadyen 2011; Gaburov et al. 2012; Vandenbroucke & De Rijcke 2016) that render fluid evolution on a dynamically moving unstructured mesh. AREPO retains accurate treatment of shocks and instabilities as well as negligible artificial viscosity that Eulerian grid codes feature, while gaining the automatic refinement and Galilean invariance inherent to SPH. These features, coupled with a tree-based self-gravity solver, make it highly attractive for a diversity of astrophysical simulations (eg. Vogelsberger et al. 2012; Pakmor & Springel 2013; ?; Marinacci

et al. 2014; Ohlmann et al. 2016), and, with the notable exception of formal angular momentum conservation, ideal for simulating WD mergers. AREPO has already been used to investigate helium detonations during the initial mass transfer phase of a 0.9 - 1.1  $M_{\odot}$  CO WD merger (Pakmor et al. 2013).

In this work, we compare the merger of a 0.625 – 0.65  $M_{\odot}$  CO WD binary system simulated in the SPH code GASOLINE (Wadsley et al. 2004) with one simulated in AREPO. We generate identical initial conditions for both simulations, and disable chemical and nuclear evolution to focus solely on the hydrodynamic differences. The purpose of this work is not to compare SPH to AREPO in the abstract, but rather to understand if any critical hydrodynamic phenomena is missing or misrepresented from past SPH-based merger simulations. We find the two simulations closely resemble one another until coalescence, after which the GASOLINE merger remnant becomes axisymmetric over  $\sim 10^2$  s, while the AREPO one remains highly asymmetric for much longer, potentially altering post-merger evolution. This work is also a companion to Zhu et al. (2015; henceforth Z15), which presents the growth of a seed magnetic field inserted into the AREPO merger to amplitudes of  $\sim 10^{10} – 10^{11}$  G at saturation, which also has significant consequences to post-merger evolution.

In Section 2, we review the formulation of SPH and AREPO, and discuss the parameters and initial conditions used in each simulation. In Section 3, we summarize efforts to improve angular momentum conservation within AREPO, essential to both this work and Z15. In Section 4, we present the results for each code and compare their outcomes. Lastly, in Section 5, we describe which code represents the more physical result, possible causes for the differences between the results, and implications for merger outcomes.

## 2. CODES AND INITIAL CONDITIONS

To better understand both the code comparison in this chapter, as well as prefacing some of our future discussion, we present an extremely short and mostly qualitative discussion on the operating principles of smoothed particle and moving mesh hydrodynamics. The historical development of both methods is long and involved, and, as improving hydrodynamic simulations is not the focus of this thesis, we refer the reader to review articles referenced throughout this section for further reading.

We write the equations of ideal magnetohydrodynamics in their conservative form and with Gaussian units (eg. Goedbloed & Poedts 2004; Pakmor & Springel 2013, Feiden & Chaboyer 2012 Sec. 3),

$$\begin{aligned} \partial_t \rho + \partial_j (\rho u^j) &= 0 \\ \partial_t (\rho u^i) + \partial_j (\rho u^i u^j + \delta^{ij} P_{\text{tot}} - \frac{1}{4\pi} B^i B^j) &= \rho \partial^i \Phi \\ \partial_t (\rho e) + \partial^j \left( u_j (\rho e + P_{\text{tot}}) - \frac{B_j}{4\pi} (u^l B_l) \right) &= u_j \rho \partial^j \Phi \\ \partial_t B^i - \partial_j (u^i B^j - u^j B^i) &= 0, \end{aligned} \quad (1)$$

where  $\rho$ ,  $u^i$ ,  $B^i$ , and  $\Phi$  are the density, velocity, magnetic field and gravitational potential, respectively,  $P_{\text{tot}} = P + \frac{1}{8\pi} B_j B^j$  is the total pressure,  $e = \frac{1}{2} u_i u^i + e_{\text{int}} + \frac{B^2}{8\pi \rho}$  is the specific total energy, and the usual Einstein summation convention holds. This can be written in compact form:

$$\frac{\partial \mathbf{U}}{\partial t} + \nabla \cdot \mathbf{F}(\mathbf{U}) = \mathbf{G} \quad (2)$$

where

$$\mathbf{U} = \begin{pmatrix} \rho \\ \rho \mathbf{u} \\ \rho e \\ \mathbf{B} \end{pmatrix}, \quad (3)$$

$$\mathbf{F}(\mathbf{U}) = \begin{pmatrix} \rho \mathbf{u} \\ \rho \mathbf{u} \mathbf{u}^T + P_{\text{tot}} - \frac{1}{4\pi} \mathbf{B} \mathbf{B}^T \\ \mathbf{u}(e + P_{\text{tot}}) - \mathbf{B} \frac{4\pi}{\rho} (\mathbf{u} \cdot \mathbf{B}) \\ \mathbf{B} \mathbf{u}^T - \mathbf{u} \mathbf{B}^T \end{pmatrix}, \quad (4)$$

$$\mathbf{G} = \begin{pmatrix} 0 \\ \rho g^i \\ u_j \rho g^j \\ 0 \end{pmatrix} \quad (5)$$

### 2.1. A Primer on Traditional Smoothed-Particle Hydrodynamics

XXXXXXXXXXXXXXXXXXXXXX

### 2.2. GASOLINE SPH Code

GASOLINE is a modular, tree-based SPH code that we previously used to explore the parameter space of CO WD mergers in Zhu et al. (2013; henceforth Z13). Code settings and initial conditions used in this work are nearly identical to those used in Z13, and we refer the reader to that paper for further details. We utilize GASOLINE’s default Hernquist & Katz (1989) kernel with 100 neighbours, and use the asymmetric energy formulation (Wadsley et al., Eqn. 8) to time-evolve particle internal energy. Artificial viscosity is provided using the standard Monaghan & Gingold formulation (see Monaghan 2005), and dynamically controlled using a combination of a Balsara (1995) switch and time-variable coefficients (eg. Dolag et al. 2005) for the linear  $\alpha$  and quadratic  $\beta$  viscosity terms ( $\alpha = 0.05$ ,  $\beta = 0.1$  when shocks are not present, and approximately unity when they are). We utilize the Helmholtz equation of state<sup>2</sup> (EOS; Timmes & Swesty 2000) to properly represent arbitrarily degenerate and relativistic gases. Since GASOLINE evolves density and entropy, while Helmholtz uses density and temperature, a Newton-Raphson inverter is included in the EOS to determine the latter from the former. To keep the energy-temperature relation positive-definite for the inverter, we enable Coulomb corrections even when the total entropy becomes negative. SPH noise occasionally brings highly degenerate particles to below the Fermi energy. Under these conditions we set the pressure to the Fermi pressure, but let the energy freely evolve (see Zhu et al. 2013, Sec. 4.6).

Like in our previous work, we ignore outer hydrogen and helium layers, composition gradients, and any nuclear reactions, in order to focus on the merger hydrodynamics. Previous work that did include nuclear reactions (Lorén-Aguilar et al. 2009; Dan et al. 2012), and in one case an outer helium layer (Raskin et al. 2012), have shown that they play a negligible role in the hydrodynamics of a 0.625 – 0.65  $M_{\odot}$  CO WD merger. More massive binaries, as well as less massive ones involving a CO-He hybrid WD, may experience He or CO

<sup>2</sup> Available at <http://cococubed.asu.edu/>.

detonations during the merger (Pakmor et al. 2010; Raskin et al. 2012; Dan et al. 2012).

We use the same version of GASOLINE as Z13, which does not include the improvements recently introduced in GASOLINE2 (Keller et al. 2015; Tamburello et al. 2015) and CHANGA/GASOLINE (Governato et al. 2015). These include a turbulent diffusion scheme to facilitate fluid mixing (Shen et al. 2010) and the use of a geometric density-averaged term in the SPH force expression (Keller et al. 2014; practically equivalent to the pressure-entropy formulation of Hopkins (2013)) to eliminate numerical surface tension at contact discontinuities, which collectively allow for proper growth of hydrodynamic instabilities. We also do not consider more advanced prescriptions for viscosity, such as a physical viscosity alongside an inviscid SPH code (eg. Lanzaflame 2003) or a Godunov-SPH scheme (eg. Cha & Wood 2016); these are generally not implemented in SPH codes. We again stress that the purpose of this work is to compare the “classical” SPH formulation, used in most merger simulations to date, to moving mesh AREPO, and we leave comparisons with improved and modified SPH schemes to future work.

### 2.3. AREPO Moving Mesh Code

We now introduce the moving-mesh magnetohydrodynamics methods of AREPO, summarizing Springel (2010a), Pakmor et al. (2011) and ?. This will be done more detail than for SPH to preface the discussion of numerical issues in Sec. 3.

AREPO discretizes a fluid using an unstructured mesh. The mesh is constructed by Voronoi tesselation of a set of mesh generating points, and these points are given velocities to follow local fluid motion in a Lagrangian fashion. This results in a mesh that deforms over time to track the evolution of the fluid, without the mesh-tangling effects that hindered previous moving mesh schemes. Mesh generating point velocities are slightly altered from their pure Lagrangian values to keep the Voronoi mesh regular, reducing flux calculation errors. Additional velocity adjustments can be made to keep cells near a constant mass or volume, but in practice this becomes ineffective for highly non-linear flows. Fluid fluxes between cells are calculated using a second-order Godunov scheme with an exact Riemann solver (in our case HLLD), while self-gravity is handled using a TreePM solver, nearly identical to the one used by SPH code GADGET2 (Springel 2005).

#### SOME STUFF ABOUT THE MESH; ASK RUEDIGER ABOUT HOW MHD WORKS!!!

On this mesh, AREPO tracks the finite volume integral of  $\mathbf{U}$  for each cell, i.e.

$$\mathbf{Q} = \int_V \mathbf{U} dV = \begin{pmatrix} m \\ \mathbf{p} \\ E \\ \mathbf{BV} \end{pmatrix}, \quad (6)$$

where  $m$  is the cell mass,  $\mathbf{p}$  its momentum,  $E$  its total energy and  $\mathbf{BV}$  the magnetic field multiplied by the cell volume ( $\mathbf{BV}$ ). If the divergence-cleaning method of Pakmor et al. (2011) is adopted, an additional scalar quantity is appended to  $\mathbf{Q}$  and to  $\mathbf{W}$ , below, but the overall equations remain unchanged (see Ch. XXX). The time-evolution for cell  $i$  from timestep  $n$  to  $n+1$  is then given by

$$\mathbf{Q}_i^{n+1} = \mathbf{Q}_i^n - \Delta t \sum_j A_{ij} \hat{\mathbf{F}}_{ij}^{n+1/2} \quad (7)$$

where  $\Delta t$  is the timestep,  $j$  stands for all cells that border cell

$i$ ,  $A_{ij}$  is the oriented area of the face dividing cells  $i$  and  $j$  and  $\hat{\mathbf{F}}_{ij}$  is the estimated flux between them (positive flux means escaping from  $i$ ). In practice fluxes are more easily calculated using primitive variables

$$\mathbf{W} = \begin{pmatrix} \rho \\ \mathbf{v} \\ P \\ B \end{pmatrix}, \quad (8)$$

then converted back to  $\mathbf{Q}$ . Fluxes are calculated in the frame of face  $A_{ij}$  (then boosted back into the simulation frame of reference) to maintain Galilean invariance. This means that each hydrodynamic step first calculates the Voronoi mesh and assigns velocities  $\mathbf{w}_i$  to the mesh-generating points before calculating  $\mathbf{W}$  and  $\hat{\mathbf{F}}$  and then advancing time using Eqn. 7 (see Springel (2010a), Sec. 3). Under standard AREPO operation,  $\mathbf{w}_i$  is the same as cell fluid speed  $\mathbf{v}_i$ , with a small corrective term to keep the mesh regular, but  $\mathbf{w}_i$  could also be set to zero, turning AREPO into a static unstructured-grid code.

Once the velocities are set, the flux across  $A_{ij}$  can be determined from the (boosted) primitive values at either side – which we term the “left” and “right” states, respectively – of the face’s centroid. In AREPO’s original formulation (Springel 2010a), these values are determined from their respective cell’s  $\mathbf{W}$  using the MUSCL-Hancock approach of a piecewise linear spatial reconstruction and a first-order time-extrapolation by half a timestep:

$$\mathbf{W}_{L,R}^{\text{interface}} = \mathbf{W}_{L,R} + \frac{\partial \mathbf{W}}{\partial \mathbf{r}} \Big|_{L,R} (\mathbf{f} - \mathbf{s}_{L,R}) + \frac{\partial \mathbf{W}}{\partial t} \Big|_{L,R} \frac{\Delta t}{2}, \quad (9)$$

where  $f$  is position of  $A_{ij}$ ’s centroid, and  $s$  each cell’s center-of-mass. The temporal gradient can be solved using the spatial gradient through the Euler equations, while the spatial gradient is estimated by taking advantage of the Green-Gauss theorem (the surface integral of a scalar field  $\phi$  is equal to the volume integral of its divergence):

$$\langle \nabla \phi \rangle_i = \frac{1}{V_i} \sum_j \phi(\mathbf{f}_{ij}) \mathbf{A}_{ij}, \quad (10)$$

taking advantage of the Voronoi mesh to estimate  $\phi(\mathbf{f}_{ij})$ . Once calculated, the gradient estimate is slope-limited before being used in Eqn. 9 (Springel (2010a) Eqns. 28 - 30). The flux is then resolved from  $\mathbf{W}_{L,R}^{\text{interface}}$  with a Riemann solver (in all our simulations, HLLD; Miyoshi & Kusano 2005). Eqns. 9 and 10 were replaced in Pakmor et al. (2016) order to resolve AREPO’s angular momentum conservation issue, but the overall flux calculation procedure remains the same as above.

The self-gravity term  $\mathbf{G}$  can easily be added to the flux calculation, since, when calculating with  $\mathbf{W}$ , gravity only changes the momentum. This change, and the corresponding one for kinetic energy, can then be appended to  $\mathbf{Q}$  (Springel 2010a Sec. 5.2).

We use the same Helmholtz EOS in AREPO that we installed into GASOLINE and also ignore composition gradients and any nuclear reactions. To assure a reasonably constant mass resolution (and other, similar criteria), we use an explicit refinement scheme (Vogelsberger et al. 2012) that adds or subtracts mesh-generating points to the grid. This keeps cell masses near a fixed value, and to keep all cell volumes within one order of magnitude of each other.

#### 2.4. Initial Conditions and Completion Time

Our chosen WD masses are typical of the narrowly peaked empirical mass distribution of field CO WDs (Tremblay & Bergeron 2009; Kleinman et al. 2013). As in Z13, we generated WDs by rescaling a sphere of particles to the proper enclosed mass-radius relation determined from 1D hydrostatic integration. We used a 50% C, 50% O composition by mass uniform throughout the star, and assumed a uniform temperature of  $5 \times 10^6$  K. The stars were placed into GASOLINE for approximately 11 dynamical times (33.3 s for the  $0.625 M_\odot$  WD and 31.3 s for the  $0.65 M_\odot$  WD). Thermal energy and particle velocity were damped to  $\sim 5 \times 10^6$  K and  $0 \text{ cm s}^{-1}$  during the first dynamical time, and left free during the remaining 10 dynamical times. 64 neighbours, rather than 100, were used during relaxation to minimize the number of particle pairs generated. These pairs (ex. Dehnen & Aly 2012, Springel 2010b) do not change global properties of the relaxed WDs, but do effectively reduce spatial resolution and having too many of them make transferring SPH initial conditions into AREPO problematic. Following relaxation, the density profile of both stars were consistent with the hydrostatic equilibrium solution, with the numerical central densities deviating from the 1D integrated ones by less than 1%. Since all particles have identical mass, the tenuous outer layers of the WDs are difficult to capture in GASOLINE; consequently the radii of the relaxed stars, as defined by the outermost particle, were  $\sim 4\%$  smaller than the integrated ones. Even after energy damping, particle noise prevents the central temperature of the relaxed stars from reaching below  $\sim 1 \times 10^7$  K, so all particle temperatures were artificially reset to  $\sim 5 \times 10^6$  K.

We then placed the relaxed stars in a circular, unsynchronized binary, with initial separation  $a_0 = 2.2 \times 10^9$  cm chosen (using the approximation of Eggleton 1983) so that the  $0.625 M_\odot$  donor will just overflow its Roche lobe.<sup>3</sup> The corresponding orbital period is 49.5 s. These initial conditions do not account for the tidal bulges of the stars, and so are not fully equilibrated (eg. Dan et al. 2011). While this means our initial conditions do not reflect “real” CO WD binaries with complete accuracy, we stress that the purpose of this work is to discover any code dependence on merger evolution, rather than providing the final word in WD merger simulations.

We generate initial conditions in AREPO by converting the SPH particles of the GASOLINE initial conditions to be mesh-generating points, while retaining their conservative quantities (mass, momentum and energy). These initial conditions are not guaranteed to be regular, but AREPO regularizes the mesh over just a few timesteps by nudging each cell’s mesh-generating points to their cell’s center of mass.

Our SPH particles all have the same mass of  $2 \times 10^{27}$  g ( $1.3 \times 10^6$  particles are needed to represent the system), comparable to the highest resolutions used in other recent work (Pakmor et al. 2012; Raskin et al. 2014). We likewise use the AREPO refinement scheme’s to keep cell masses within a factor of 2 of this value, and to keep adjacent cell volumes to within a relative factor of 10. We additionally initialize a background grid of  $10^{-5}$  gcc cells in AREPO to fill the vacuum surrounding the WDs – this adds only  $0.005 M_\odot$  of material to the simulation. Consequently, our spatial resolution

<sup>3</sup> The hydrostatic equilibrium solution radius was used to calculate  $a_0$ , rather than the smaller relaxed SPH star radius. This accounts for the small differences in initial conditions between this work and the equivalent simulation in Z13.

in GASOLINE is about a factor of 3 lower than that in AREPO but because the two codes differ so greatly regardless of resolution, we believe equivalent mass resolution to be the most appropriate comparison (see Vogelsberger et al. Sec. 2.3 for complications in achieving equivalent accuracy in SPH and grid codes). AREPO’s grid refinement scheme also naturally increases the resolution of our simulations over time, and so all AREPO resolutions stated are for the start of the simulation. In Sec. 5.1 we check if our results are resolution-dependent.

We run both simulation to 1000 s. For the GASOLINE simulation, this is long after its hydrodynamic evolution has completed, at  $\sim 400$ s, and it begins a phase of slow secular spin-down due to artificial viscosity redistributing angular momentum. Hydrodynamic evolution has also ended for the AREPO simulation by  $\sim 400$ s, and the merger remnant also subsequently evolves much more slowly, but, as we shall see in Sec. 4, this further evolution is also hydrodynamic.

#### 3. THE ROAD TO IMPROVING ANGULAR MOMENTUM CONSERVATION IN AREPO

The first simulation we performed in AREPO showed dramatic differences from our GASOLINE ones. In it, the  $0.625 M_\odot$  donor WD is destroyed by tidal forces within  $\sim 3$  orbital periods ( $\sim 150$ s), versus the GASOLINE simulation’s  $\sim 4$  ( $\sim 200$ s). Following coalescence, the AREPO simulation featured a dense, crescent-shaped region formed from accretor material, retaining its pre-merger temperature of  $\sim 10^7$  K, while the GASOLINE merger remnant was relatively hot throughout its interior, with an average temperature of  $\sim 2 \times 10^8$  K. Most prominently, the GASOLINE remnant evolved into an axisymmetric configuration  $\sim 250$  s after coalescence while the AREPO remnant maintained the integrity of its non-axisymmetric crescent while launching one, and then multiple trailing spiral waves into the surrounding medium. Over  $\sim 10^3$  s, the angular velocity of the entire remnant dropped to zero. Spiral waves – hitherto unmentioned in WD merger literature (though frequently discussed in the context of accretion disks) – are a mechanism for transporting angular momentum (eg. Papaloizou & Lin 1995; Balbus 2003) and was initially presumed to be the cause of this remnant spin-down. Global angular momentum, however, was not conserved, and in this section we summarize our attempts at isolating the cause of this angular momentum leak, and which features discussed above turned out to be spurious once the leak was plugged.

In the top panel of Fig. 1, we plot both the total  $z$ -axis angular momentum  $L_{z,\text{tot}}$  and that within a cylinder oriented along the rotational axis and with radius  $\varpi = 10^9$  cm, which we denote  $L_{z,\varpi < 9}$ , for low-resolution ( $1 \times 10^{28}$  g, or  $2.5 \times 10^5$  particles/cells at the start of simulation) and standard-resolution ( $2 \times 10^{27}$  g) GASOLINE and AREPO simulations. Because coalescence occurs at different times between them, we shift each simulation’s curve so that  $t = 0$  corresponds to the “coalescence time”, defined as the time in each simulation when  $L_{z,\varpi < 9}$  achieves its maximum value. SPH formally conserves angular momentum, and we find the  $L_{z,\text{tot}}$  for GASOLINE varies in time by  $\lesssim 10^{-5}$  its mean value at either resolution. On the other hand, the AREPO low-resolution simulation loses a *third* of its angular momentum over  $\sim 1000$ s, and the standard-resolution one  $\sim 20\%$ .

A moving mesh that refines in regions of high density may not properly resolve the outer regions of the simulation, where the momentum appeared to be carried, nor low-density but high-energy (and thus dynamically important) regions near

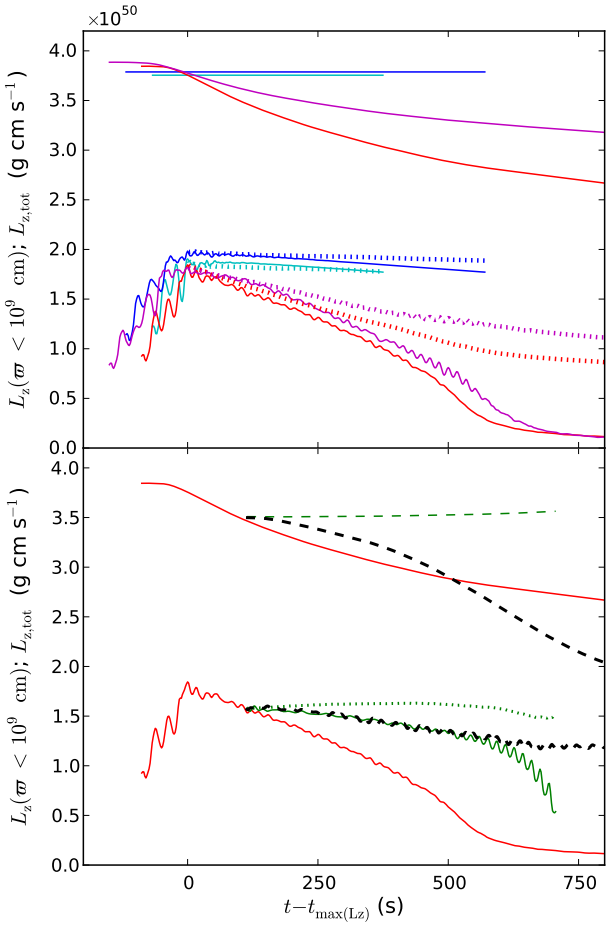


**Figure 1.** Time evolution of total  $z$ -axis angular momentum  $L_{z,\text{tot}}$  (top cluster of lines in each panel) and that within a cylinder of radius  $\varpi = 10^9 \text{ cm}$ ,  $L_{z,\varpi < 9}$  (bottom cluster), for various simulations in 2013-2014.  $t = 0$  is defined as the time in each simulation when  $L_{z,\varpi < 9}$  achieves its maximum value. In the top panel, red and magenta lines represent the low and standard-resolution AREPO simulations, respectively, while the cyan and blue ones represent low and standard-resolution GASOLINE ones, respectively. Dotted lines represent angular momentum balance  $L_{\text{bal}}(\varpi < 10^9 \text{ cm})$ , which should be flat in the absence of spurious angular momentum losses; colors correspond to their respective simulations. Different initial amounts of total angular momentum between AREPO and GASOLINE runs is due to inconsistencies in their initial conditions that have subsequently been solved. In the bottom panel, the red line is again the low-resolution AREPO simulation, while the green line is for an AREPO low-resolution run where the mesh is held static after  $t = 114 \text{ s}$  (dotted line represents angular momentum balance). The dashed black line is a FLASH simulation that uses the AREPO low-resolution run at  $t = 114 \text{ s}$  for initial conditions; its loss of total angular momentum is due to having outflow boundaries.

the center, such as the hot, low-density vortex encapsulated by the dense crescent. To better pinpoint where in the system the angular momentum is being spuriously lost, we compute (similar to Ji et al. (2013) Sec. 2.2.4) the theoretically expected change in  $z$ -angular momentum. For a cylinder  $V$  oriented along the rotational axis, this is given by (via the Euler equations)

$$\frac{\partial L_z}{\partial t} = - \oint_V \rho \varpi v_\phi v_\varpi dS + \int_V \varpi \times \nabla \Phi dV \quad (11)$$

where the first term encapsulates advection (including wave motion; eg. Balbus 2003) out of the volume and the second

external torque – in our case gravitational.<sup>4</sup> Subtracting the time-integral of Eqn. 11 (i.e. the cumulative angular momentum change  $\Delta L_z$ ) from the volume’s angular momentum gives us the “balance”

$$L_{\text{bal}}(t) = L(t) - \Delta L_z = L(t) - \int_{t_0}^t \frac{\partial L_z}{\partial t'} dt'. \quad (12)$$

In a system with perfect angular momentum conservation,  $L_{\text{bal}}(t) = L_{\text{bal}}(t_0)$ . In Fig. 1  $L_{\text{bal}}$  for a cylinder of  $\varpi = 10^9 \text{ cm}$  is plotted as a dashed line for each simulation. While  $L_{\text{bal}}(\varpi < 10^9 \text{ cm})$  decreases by  $\sim 5\%$  for the GASOLINE simulations (likely due to artificial viscosity, not included in Eqn. 11), the change in  $L_{\text{bal}}$  accounts for approximately *all* of the total spurious losses in AREPO (compare the  $L_{z,\text{tot}}$  and  $L_{\text{bal}}$  lines), invalidating the hypothesis that it is the outer regions of the simulation spuriously losing angular momentum.

To test whether the low-density, high-energy regions near the center were underresolved, we added a volume refinement criterion for cells within  $\varpi = 10^9 \text{ cm}$  that activates once more than 75% of the system’s mass is within this boundary; This translated to a dramatic increase in resolution over time, with the simulation eventually exceeding  $2 \times 10^7$  grid points. This run loses  $\sim 5\%$  of  $L_{z,\text{tot}}$  in  $\sim 500 \text{ s}$ , but  $\sim 30\%$  of  $L_{z,\varpi < 9}$  is still spuriously lost over the same timespan, meaning spurious losses would only be rendered negligible at impractically high resolutions.

In the bottom panel of Fig. 1, we plot a simulation performed in the Eulerian code FLASH (Fryxell et al. 2000, DUBEY+09 from KASHYAP+15), using the low-resolution AREPO run at  $t = 110 \text{ s}$  (chosen to be  $\sim 2$  orbital periods after coalescence) for initial conditions. We used a 3D Cartesian grid of size  $1.6 \times 10^{10} \text{ cm}$  to a side, with multiple levels of fixed-mesh refinement centered on the newly-formed merger remnant such that its core is resolved with cells  $7.8 \times 10^6 \text{ cm}$  to a side (comparable to low-resolution AREPO’s  $\sim 10^7 \text{ cm}$  in the core). Gravity was solved using the multiple solver with  $l_{\text{max}} = 50$ , and fluxes propagated with the HLLC Riemann solver. We also plot a low-resolution AREPO run where, at  $t = 110 \text{ s}$  the mesh’s velocities were forced to zero, transforming AREPO into a static grid code operating on an unstructured mesh. Considering the sheer number of differences between the two codes, their simulations agree remarkably with one another on the rate of change of  $L_{z,\varpi < 9}$  until very late times (when the remnant drifted away from the AREPO static mesh). **Both also conserve total angular momentum to within  $\sim 2\%$** , and  $L_{\text{bal}}(\varpi < 10^9 \text{ cm})$  for the AREPO-static run changes by  $\sim 1\%$  over  $\sim 500 \text{ s}$ .<sup>5</sup> These simulations suggested AREPO’s moving mesh scheme cause spurious angular momentum losses.

Eventually, two aspects of AREPO’s original hydrodynamic scheme (Sec. 2.3) responsible for making the code only *first-order* convergent for non-trivial moving meshes were pinpointed and revised; this is detailed in ?, which we now sum-

<sup>4</sup> A third, pressure torque term also arises in general, but for an axisymmetric volume it is analytically zero (and numerically negligible as well).

<sup>5</sup> We also attempted to transport AREPO simulation snapshots following coalescence into GASOLINE, and vice versa. The former showed angular momentum transport and the spiral pattern fading away within  $\sim 150 \text{ s}$ , while the latter showed the onset of Kelvin-Helmholtz instabilities at the interface between the rigidly rotating and sub-Keplerian portions of the remnant, followed by angular momentum loss. This was the case even when the GASOLINE initial conditions were nearly axisymmetric, and stable to hydrodynamic instability by Maeder et al. (2013)’s modified Solberg-Hoiland criterion.

marize. First, while Eqn. 9 provides second-order convergence on static meshes of arbitrary geometry, it only uses the initial state of the mesh itself, and so only provides first-order convergence on moving meshes. Second, AREPO’s estimate for  $\phi(\mathbf{f}_{ij})$  in Eqn. 10 assumes that the cell centers of mass  $\mathbf{s}$ , where the value of  $\mathbf{W}$  is defined, and mesh-generating points  $\mathbf{r}$  align, which is untrue for severely distorted meshes. This first-order convergence does not inevitably cause major errors – indeed, ? finds it does not affect their galaxy formation studies (eg. ?) – but for a rotation-dominated system being simulated over hundreds of dynamical times, such as the accretion disk in ?, systematic deviations in angular momentum conservation become apparent.

The solution is also two-fold: first, replace Eqns. 7 and 9 by a hybrid MUSCL-RK2 method:

$$\begin{aligned} \mathbf{W}'_i &= \mathbf{W}_i^n + \Delta t \frac{\partial \mathbf{W}}{\partial t} \\ \mathbf{r}' &= \mathbf{r}^n + \Delta t \mathbf{w}^n \\ \mathbf{Q}_i^{n+1} &= \mathbf{Q}_i^n - \frac{\Delta t}{2} \left( \sum_j A_{ij}^n \hat{\mathbf{F}}_{ij}^n(\mathbf{W}^n) + \sum_j A'_{ij} \hat{\mathbf{F}}_{ij}'(\mathbf{W}') \right) \\ \mathbf{r}^{n+1} &= \mathbf{r}', \end{aligned} \quad (13)$$

where  $\mathbf{r}$  is the coordinate of the mesh-generating point. With this method, we first make a prediction of the cell’s future primitive variables  $\mathbf{W}'$ , as well as the future Voronoi mesh. We then use both the current and predicted values to calculate an average flux and time-evolve the cell. **Spatial extrapolation to the cell interface is implicit when calculating  $\hat{F}_{ij}$ ?** The mesh velocities are assumed constant over  $\Delta t$ , so the predicted and true future mesh are identical. Second, the Green-Gauss gradient estimate is replaced with linear least-squares estimator, where slope  $\langle \nabla \phi \rangle_i$  is determined by minimizing

$$\sum_j g_j (\phi_j - \phi_i - \langle \nabla \phi \rangle_i (\mathbf{s}_j - \mathbf{s}_i))^2, \quad (14)$$

where  $g_j \equiv A_{ij}/|\mathbf{s}_j - \mathbf{s}_i|^2$  is a weighting function. This estimate gives the value that best reproduces the change in  $\phi$  when travelling from cell  $i$  to any of its neighbours, and relies only on cell centers of mass (and their values of  $\mathbf{W}$ ), rather than mesh generating points. Working in concert, these “RKLSF” fixes allow AREPO to become second-order convergent.

In Fig. 2, we show angular momentum evolution for AREPO-RKLSF runs (from Sec. 5.1) at resolutions ranging from  $5.1 \times 10^4$  to  $2.5 \times 10^6$  cells. In all but the lowest-resolution run,  $L_{z,\text{tot}}$  deviates by less than  $\sim 7\%$  from its initial value, and at the highest resolution run of  $2.5 \times 10^6$  cells, it deviates by  $\sim 1\%$  over  $\sim 840$ s, an order of magnitude better than the  $2 \times 10^7$ -cell simulation without the RKLSF implementation. Also, in all but the lowest-resolution run, the spin-down of the remnant core is orders of magnitude slower (discussed further in Sec. ??), cementing the fact that the rapid spin-down seen in Fig. 1 was an artefact of spurious angular momentum losses. We now compare these AREPO-RKLSF simulations against ones in GASOLINE.

#### 4. RESULTS

Fig. 3 compares snapshots at various times in the GASOLINE and AREPO simulations.

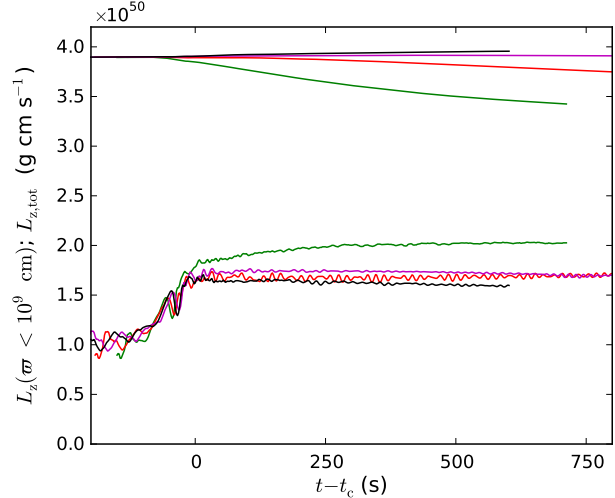


**Figure 2.** Time evolution of total  $z$ -axis angular momentum  $L_{z,\text{tot}}$  (top cluster of lines) and that within a cylinder of radius  $r = 10^9$  cm,  $L_{z,r<9}$  (bottom cluster) for the AREPO-RKLSF simulations. Colors indicate initial resolution: green is for  $5.1 \times 10^4$  cells, red for  $2.5 \times 10^5$ , magenta for  $1.3 \times 10^6$  and black for  $2.5 \times 10^6$ .

The initial evolution of the two systems, shown in row 1 of Fig. 3, is qualitatively similar. Our initial conditions are approximate, so both stars immediately tidally stretch in response to the binary potential, overshooting their Roche lobes in the process and transferring mass to each other in spurts. This eventually dies down for the  $0.65 M_\odot$  accretor, and becomes steady mass transfer for the  $0.625 M_\odot$  donor, just prior to it becoming fully disrupted. In reality, the  $0.625 M_\odot$  donor WD should overflow first and begin a period of quasi-stable mass transfer over potentially dozens of orbits, and so our simulations, both of which experience donor full disruption in just a few orbits, overestimate the rate of early mass transfer (Dan et al. 2011).

The accretion streams in both codes are travelling at supersonic speeds ( $\mathcal{M} \approx 2$ ) relative to the accretor when they impact, and as a result the streams shock-heat at impact and their material rapidly thermalize. By the time the donor is fully disrupted a hot atmosphere has formed around the accretor. This atmosphere has a temperature of  $1.6 \times 10^8$  K in AREPO and  $1.9 \times 10^8$  K in GASOLINE – both about half of the virial temperature,  $GM_a m_p / 3R_d k_B \approx 4 \times 10^8$  K – with corresponding densities of  $1.8 \times 10^5$  g cm $^{-3}$  and  $2.3 \times 10^5$  g cm $^{-3}$ , respectively. As seen in Fig. 3 row 1, AREPO’s hot atmosphere is somewhat less extended and tends to have more localized hotspots in temperature compared to the extended and uniform one in GASOLINE. This may be due to a combination of AREPO being better able to capture underdense regions **DISCUSS WHY EARLIER!**, and having higher local spatial resolution for the same mass resolution

As mass transfer continues to expand the donor and draw it closer to the accretor, eventually tidal forces between the two WDs are strong enough to fully disrupt the donor, stretching it out into a thick stream of material that wraps around the donor, as seen in Fig. 3 row 1. In both simulations, this occurs  $\sim 3.7$  orbital periods of the initial binary, or  $\sim 180$ s, after the start of simulation, by which time the donor has transferred  $\sim 0.05 M_\odot$  to the accretor. During coalescence, both the density and temperature profiles appear very similar between the codes, and the destruction of the donor takes over the same

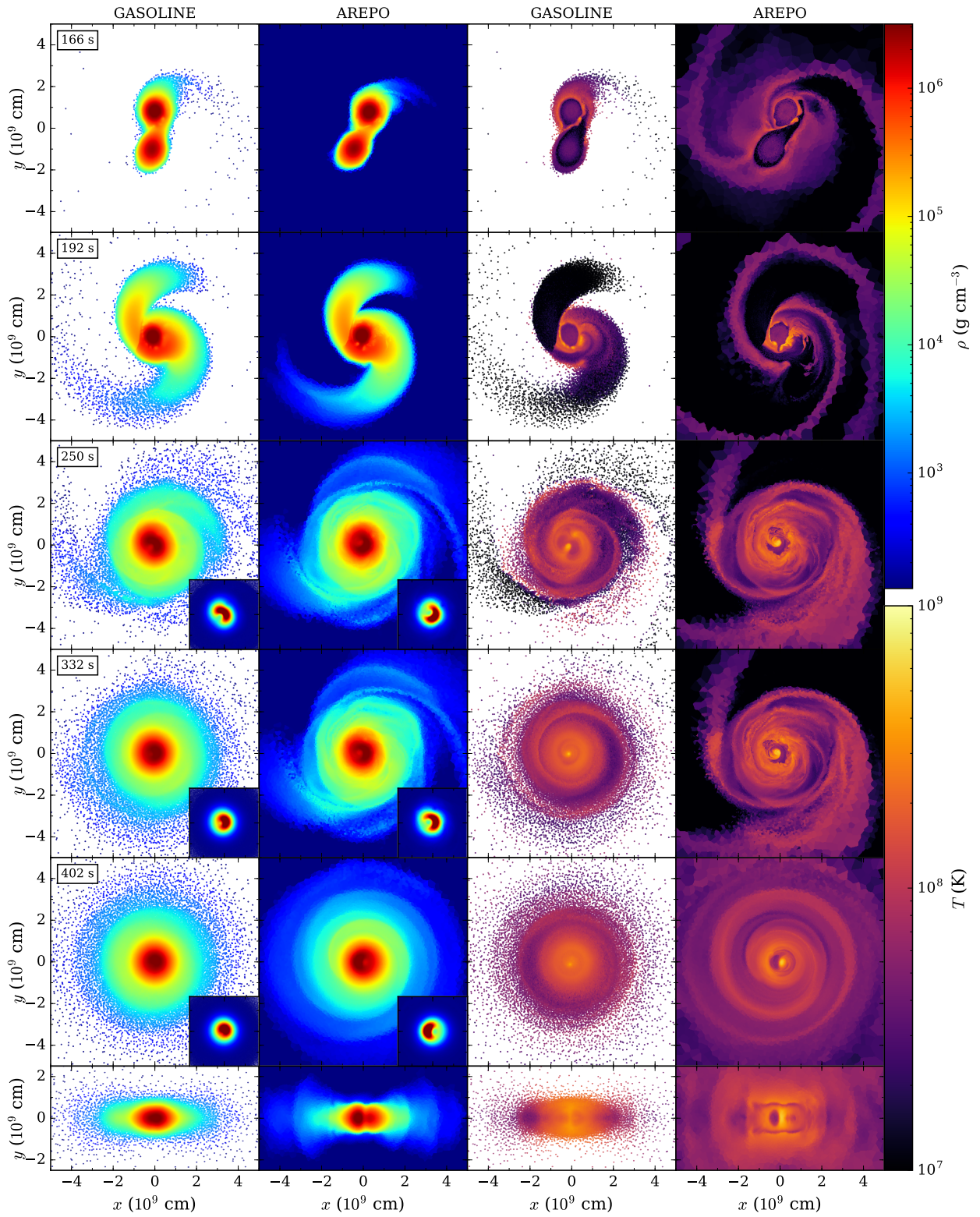


**Figure 3.** Series of equatorial (xy) plane density (left two columns) and temperature (right two columns) intensity plots for five snapshots in time (rows; the time for each snapshot is indicated at the top left of the density plots) during the GASOLINE and AREPO simulations. xz-plane plots are also included for the final snapshot.

amount of time – about one orbital period, or 49.5 s – in both codes.

Once the donor is fully disrupted, a portion of it forms an accretion stream that slides across the accretor at supersonic speeds, creating a string of Kelvin-Helmholtz vortices. In AREPO these vortices are markedly more pronounced, being both larger by  $\sim 30\%$  in radius, and having a slightly higher temperature of  $\sim 5 \times 10^8$  K compared to GASOLINE’s  $\sim 4 \times 10^8$  K. The accretion stream continues to inspiral toward the center of the accretor, severely deforming the accretor while carrying the string of Kelvin-Helmholtz vortices toward the center of the system. Meanwhile, the remainder of the donor material increases its average distance from the accretor (conserving total angular momentum), wrapping around it as a thick sub-Keplerian disk. The two WDs have nearly equal masses, so material near the surface of the accretor is dredged up to become part of the disk, while the incoming donor accretion streams severely disrupt the accretor from a sphere into a crescent shape. This process, coalescence, is approximately complete when the average separation between material from the donor and accretor changes from its initial value of  $2.2 \times 10^9$  cm to its equilibrium value of  $\sim 1 - 2 \times 10^8$  cm. We thus estimate the time coalescence is complete,  $t_c$ , by determining the time when average donor-accretor separation reaches a tenth of its initial value. We find  $t_c = 228$  s for GASOLINE, and 220 s (roughly Fig. 3, row 3).

In Fig. 4, we plot profiles of density, temperature and energy for the merger remnants 99 s (2 orbital periods) after coalescence, roughly equivalent to row 4 of Fig. 3. Profiles both along the original plane of the merger, or “equatorial plane” (solid lines) and rotational axis are considered, and like Z13 we map  $\omega$  and  $z$  positions to the ratio of corresponding spherical enclosed mass to total mass  $M/M_{\text{tot}}$ . The equatorial profiles are axisymmetrically averaged, while the rotational axis ones are averaged from the profiles above and below the equatorial plane. As a whole, the two remnants have very similar structures: both feature a degeneracy-supported core surrounded by a rotationally supported thick disk along the equatorial plane (plane of the original binary), and by a hot, thermally supported atmosphere along the axis of rotation. Following Z13 Sec. 3.2.3, we find the disk mass  $M_{\text{disk}} = 0.23 M_{\odot}$  and the core-envelope mass  $M_{\text{ce}} = 1.05 M_{\odot}$  in both simulations, though we note that the core-envelope also has substantial rotational support throughout.<sup>6</sup> Both remnant’s internal energy ( $1.5 \times 10^{50}$  erg) is also identically divided into  $\sim 30\%$  rotational,  $\sim 10\%$  thermal and  $\sim 60\%$  degeneracy energy. One minor difference between the two codes is the total amount of material unbound by the merger –  $1.4 \times 10^{-3} M_{\odot}$  in GASOLINE, and  $5.0 \times 10^{-3} M_{\odot}$  in AREPO – though this value is much smaller and harder to constrain than the bulk values above.

The simulations’ profiles in Fig. 4 are likewise very similar in shape to one another: both, for example, have a peak density of  $\sim 3 \times 10^6$  g cm $^{-3}$  and a large fraction of their mass rotating nearly rigidly at  $\sim 0.3$  s $^{-1}$ . We also plot the AREPO MHD simulation from Zhu et al. (2015) in grey, and find it is also similar to both simulations, indicating that including magnetic dynamo effects lead only to minor changes in the hydrodynamics in the merger. The greatest discrepancy is in the factor of  $\sim 2$  decrease in the temperature curve at small

<sup>6</sup> The mass of material whose degeneracy specific energy is  $> 50\%$  of their total specific energy is  $\sim 0.8 M_{\odot}$  in both simulations, as in Zhu et al. (2015).

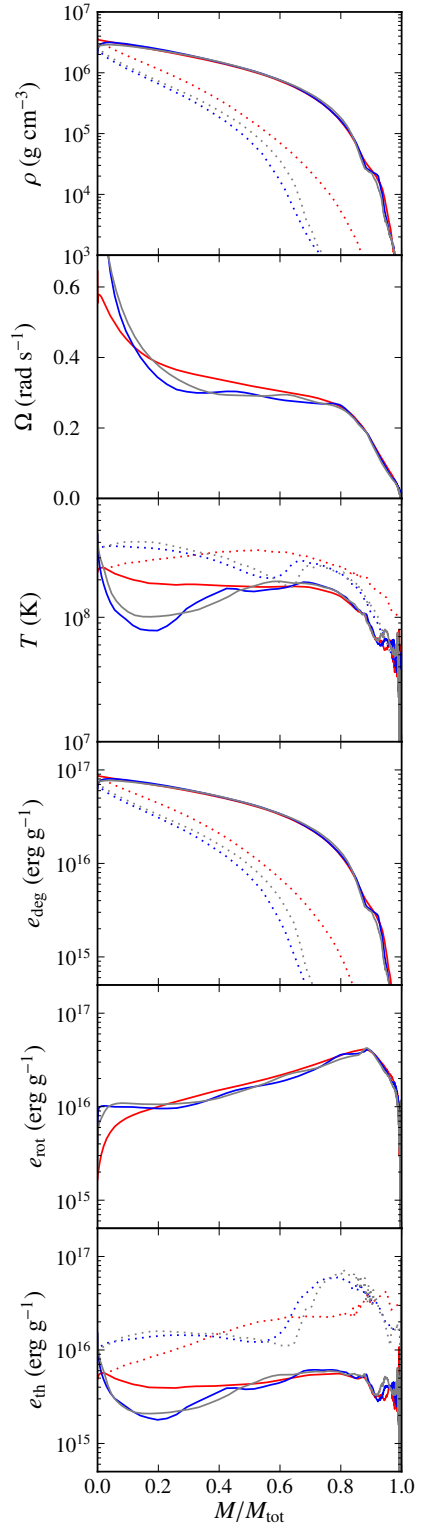


**Figure 4.** Merger remnant profiles from the GASOLINE (red), AREPO (blue) and AREPO MHD (gray; Zhu et al. 2015) simulations 99 s after coalescence (around row four of Fig. 3). The profiles are, from top to bottom, density  $\rho$ , angular rotation speed  $\Omega$ , temperature  $T$ , specific degeneracy energy  $e_{\text{deg}}$ , specific thermal energy  $e_{\text{th}}$ , and specific rotational energy  $e_{\text{rot}}$ , all as a function of the ratio of spherical enclosed to total mass  $M/M_{\text{tot}}$ . Solid lines represent profiles on the original binary’s orbital plane, while dash-dotted lines represent profiles along the rotational axis.

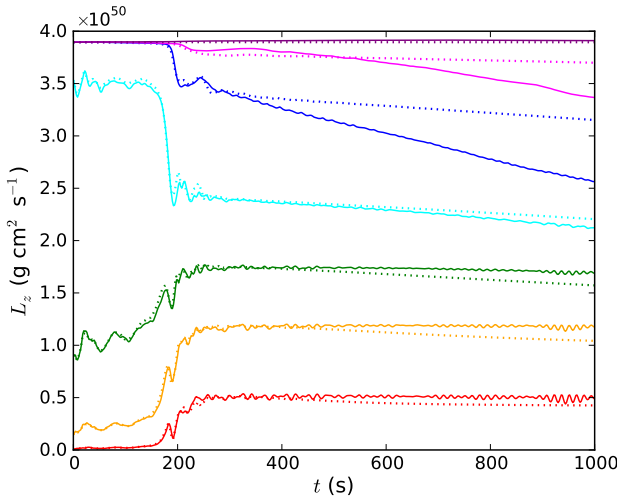


**Figure 5.** Time evolution of  $z$ -axis angular momentum  $L_z$  for AREPO (solid lines) and GASOLINE (dotted) simulations. The purple line represents total  $L_z$ , while the others represent angular momentum within concentric cylinders aligned along the rotation axis and with radii  $\varpi = 5 \times 10^8$  (red),  $7.5 \times 10^8$  (yellow),  $1 \times 10^9$  (green),  $1.5 \times 10^9$  (cyan),  $3 \times 10^9$  (blue) and  $6 \times 10^9$  cm (magenta).

$M/M_{\text{tot}}$  in the AREPO simulation.

That discrepancy, however, reflects a larger evolutionary difference visible in rows 4 - 6 of Fig. 3. Just after coalescence, the center of the merger remnant in both simulations is clearly divided into a dense and cold crescent-shaped region, formed from the perturbed core of the accreting WD, and a low-density void that is an order of magnitude hotter, formed by material roughly evenly mixed between donor and accretor (this hot void appears as a column in the  $xz$  plots of Fig. 3). 99 s after coalescence, the hot void has a density and temperature of  $\sim 2 \times 10^6 \text{ g cm}^{-3}$  and  $\sim 6 \times 10^8 \text{ K}$ , respectively, in both codes, but the AREPO void is  $\sim 80\%$  larger in radius. The cold crescent, on the other hand, has a density of  $\sim 4 \times 10^6 \text{ g cm}^{-3}$  in both codes, but has a temperature of  $\sim 2 \times 10^8 \text{ K}$  GASOLINE versus  $\sim 5 \times 10^7 \text{ K}$  in AREPO. Over the next several hundred seconds, the GASOLINE remnant's crescent deforms into something more axisymmetric and uniform in temperature, while what remains of the hot void moves off of the equatorial plane to form two hotspots along the rotational axis (row 6 of Fig. 3). By  $t \approx 500$  s, its structure has stopped evolving on a hydrodynamic timescale (roughly equal to one binary orbital period). AREPO, on the other hand, maintains the distinction between its crescent and void, and consequently remains non-axisymmetric, for more than a thousand seconds after coalescence. The system's center of rotation and mass coincide at the midpoint along the boundary between the crescent's interior edge and the hot void, and most of the dense crescent actually revolves around this point (rather than spinning about it). This generates a lopsided gravitational potential that perturbs the surrounding disk, launching a single spiral wave into the surrounding medium.

Since spiral waves transport angular momentum, we show the evolution of  $z$ -axis angular momentum  $L_z$  within concentric cylinders in Fig. 5 for the two simulations. We see that all cylinders slowly lose angular momentum after coalescence in the GASOLINE simulation, likely a consequence of artificial viscosity. The AREPO simulation's  $L_z$  within  $\varpi = 10^9 \text{ cm}$  changes by less than  $\sim 0.5\%$  over 1000 s. By

contrast the  $L_z(\varpi < 3 \times 10^9 \text{ cm})$  drops at a rate of  $dL_z/dt = 1.2 \times 10^{47} \text{ g cm}^2 \text{s}^{-2}$  (compared to the of its GASOLINE equivalent of  $3.3 \times 10^{46} \text{ g cm}^2 \text{s}^{-2}$ ). The base of the spiral wave is at  $\varpi \approx 1.5 \times 10^9 \text{ cm}$ , which suggests the  $L_z(\varpi < 3 \times 10^9 \text{ cm})$  curve probes the wave's angular momentum transport. At  $\sim 1000$  s, AREPO's simulation still resembles row 6 of Fig. 3, indicating that the crescent structure is quasi-stationary and persists on a timescale approaching the post-merger viscous timescale calculated by van Kerkwijk et al. 2010 and Shen et al. (2012). We discuss the physical robustness and implications of this result in Sec. XXX.

## 5. DISCUSSION

To determine the robustness of our results, and provide clues to the sources of the differences between AREPO and GASOLINE simulations, we ran a number of tests varying code parameters.

### 5.1. Resolution Test

As noted in Sec. 2.4, an AREPO simulation with identical mass resolution to a GASOLINE one will have roughly a factor of 3 higher spatial resolution because of the 100 neighbouring particles needed by the kernel. It is possible that the differences we observe between our simulations are not due to fundamental differences between the codes, but because our GASOLINE simulation insufficiently resolves the merger. To address this, we performed a series of GASOLINE and AREPO simulations with a mass resolutions of  $5 \times 10^{28} \text{ g}$  (equivalent to  $5.1 \times 10^4$  particles/cells and comparable to resolutions used in parameter-space sweeps Dan et al. 2012, 2014),  $1 \times 10^{28} \text{ g}$  ( $2.6 \times 10^5$ ) and  $1 \times 10^{27} \text{ g}$  ( $2.6 \times 10^6$ ). This factor of 50 range in mass resolution ( $\sim 4$  in spatial resolution) allows us to both determine the degree to which mergers in each code change with resolution, and to compare AREPO runs to GASOLINE ones at finer mass resolution.

At all four resolutions, the GASOLINE simulations exhibit very similar behaviour prior to coalescence. The donor fully disrupts in at  $\sim 3.5$  orbits of the initial binary for the two higher resolution runs, while the two lower-resolution ones experience a slightly earlier disruption at  $\sim 3.2$  orbits ( $\sim 155$ – $160$  s). Coalescence for the highest resolution run occurs at  $t_c = 230$  s, within 2 seconds of the standard resolution value, while it occurs 15–30 seconds earlier for the two lower resolution runs (we note the method we determine coalescence is somewhat sensitive to changes in the detailed configuration of the remnant). Just after coalescence, all reproduce the crescent-and-void configuration, with the void being least prominent in the lowest-resolution run. AREPO also reproduces the same qualitative evolution up to coalescence at all resolutions, but donor disruption occurs within only  $\sim 2$  orbits at its lowest resolution, and in  $\sim 3$  in its second lowest. The time of coalescence is likewise much sooner in the lowest resolution simulation, at  $t_c = 150$  s for the lowest resolution run. The two higher resolution runs, however, are very similar to one another, with donor disruption occurring at  $\sim 180$  s and  $t_c = 234$  s, much closer to the standard resolution run's values. These differences are in part due to our initial conditions setup, where GASOLINE SPH particles are directly mapped to AREPO cells. WDs that are hydrostatic in GASOLINE are not precisely so in AREPO, particularly in the poorly resolved atmosphere, and we see the WDs spuriously expanding in the first few seconds. This effect leads to larger mass-transfer rates early in the merger, and is magnified with decreasing

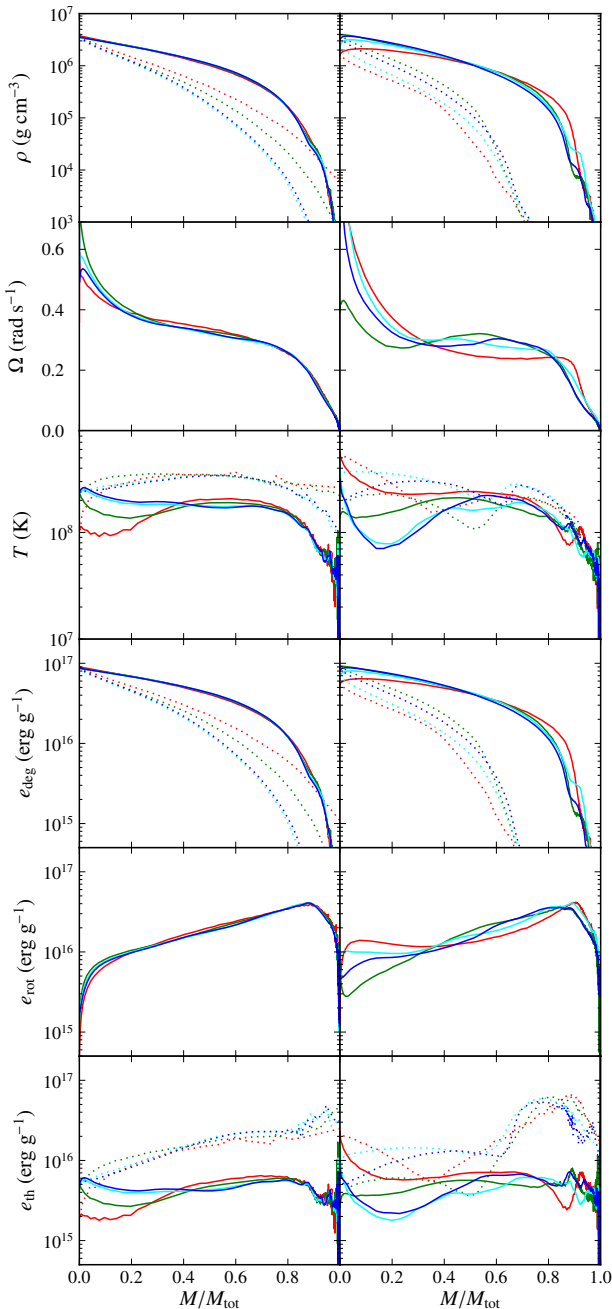


**Figure 6.** Merger remnant profiles, as in Fig. 4, for GASOLINE (left column) and AREPO (right) simulations of various (initial, for AREPO) mass resolutions. Resolutions include  $5 \times 10^{28}$  g (equivalent to  $5.1 \times 10^4$  particles/cells; red lines),  $1 \times 10^{28}$  g ( $2.6 \times 10^5$ ; green)  $2 \times 10^{27}$  g ( $1.3 \times 10^6$ ; cyan) and  $1 \times 10^{27}$  g ( $2.6 \times 10^6$ ; blue).

$\sim 3.5$

resolution. Just after coalescence, all reproduce the crescent-and-void configuration, with the void being least prominent in the lowest-resolution run.

In Fig. 6, we plot the equatorial and rotational axis profiles of all simulations 100 s after their time of coalescence. The GASOLINE remnants (left column) are all remarkably similar to one another, with the sole exception of the temperature structure at the lowest resolution. The disk and core-envelope masses as well as internal energy and its partitioning into var-

ious forms are all within 1% of their values at standard resolution reported in Sec. 4. The central density also deviates by  $\lesssim 3\%$  from  $3.6 \times 10^6$  g cm $^{-3}$  in all remnants. The AREPO remnants (right column) are less uniform: masses and energies vary by  $\sim 10\%$  from their reported values in Sec. 4, and the central density ranges from  $3-4 \times 10^6$  g cm $^{-3}$  for all resolutions except the lowest one, where it is  $\sim 2 \times 10^6$  g cm $^{-3}$ . The variations in the rotation and temperature curves reflect variations in the structure of the dense crescent and hot void. While at the highest two resolutions the dense crescent is clearly colder, with a temperature of  $\sim 6 \times 10^7$  K, at a resolution of  $1 \times 10^{28}$  g the crescent’s temperature is a much warmer  $3 \times 10^8$  K, and at the lowest resolution the remnant’s core never forms a crescent at all, instead appearing as a dumbbell-shaped object that transforms into a spherically symmetric one within 500 s of coalescence. During this time, global angular momentum decreases by  $\sim 10$  (see Fig. 2), and a  $< 10^7$  K ring of material spurious forms at the interface between donor and accretor, both indicating that the AREPO is too poorly resolved to simulate the merger. At all other resolutions, however, the crescent and void survive until the end of the simulation at 1000 s.

The crescent-void configuration also appears, but then fades away over several hundred seconds, in all GASOLINE simulations. To check if the longevity of the configuration is resolution-dependent, we turn to Zhu et al. 2013’s measurement of non-axisymmetry, measured from  $|f_1|/|f_0|$ , the ratio of largest non-zero to zeroth Fourier coefficient of particles or cells binned in azimuth. For all simulations, the largest non-zero Fourier coefficient is the first, and the time the hot void disappears the remnant roughly matches the time  $t_f$  when  $|f_1|/|f_0| = 0.01$ . We find, from lowest to highest resolution,  $t_f = 425$  s, 483 s, 515 s and 513 s – roughly corroborated by visual inspection of the remnant’s non-axisymmetry – that suggests convergence at  $t_f \approx 510$  s. Note that all AREPO simulations maintain  $|f_1|/|f_0| \gtrsim 0.1$  for  $\gtrsim 1000$  s, except (unsurprisingly) for the lowest-resolution run, which drops to  $|f_1|/|f_0| \approx 0.02$  by the end of the simulation.

We thus conclude that the largest difference between the GASOLINE and AREPO simulations – the survival of the crescent-void configuration long after the merger – is the case for all resolutions. The void persists for hundreds of seconds in all but the lowest-resolution AREPO simulations, while even in the highest-resolution GASOLINE one it smears away, disappearing within  $\sim 250$  s after coalescence. This indicates that spatial resolution alone is insufficient to explain the diverging behavior of the codes. We also find that, curiously, that GASOLINE’s results change little between all resolutions, while AREPO’s results only appear to agree at the highest resolutions. This bodes well for merger parameter-space studies using lower-resolution SPH simulations (eg. Z13, Dan et al. 2014; ?; the latter finds in their resolution study similar results unless nuclear burning becomes important during the merger), but the same study would require a mass resolution finer than  $\sim 1 \times 10^{28}$  g in AREPO (and ideally closer to our standard resolution of  $2 \times 10^{27}$  g) to guarantee qualitative accuracy with higher-resolution runs.

### 5.1.1. Varying Viscosity in GASOLINE

Artificial viscosity, which is essential in SPH for proper shock capture, has been a major issue for white dwarf merger simulations for decades (eg. Guerrero et al. 2004; Lorén-Aguilar et al. 2009) because it spuriously shears differen-

tial rotation into rigid rotation, dumping excess energy into heat. This viscosity cannot simply be mitigated by resolution Springel (2010b), and we cannot run our mergers with zero artificial viscosity without neglecting shock heating and introducing unphysical particle behaviour. We can, however, increase and reduce its strength to see what effect it has on our simulation results, as in Z13 Sec. XXX.

We ran GASOLINE simulations of our merger with a mass resolution of  $1 \times 10^{28}$  g and time-independent artificial viscosity coefficients of either  $\alpha = 0.05$ ,  $\beta = 0.1$ , or  $\alpha = 1$ ,  $\beta = 2$  (the Balsara switch is still active), comparing them to the variable-viscosity run at the same resolution in Sec. 5.1. These simulations both experience donor disruption after  $\sim 3.2$  binary orbits, similar to the variable one, and coalescence occurs at 205 s and 219 s for the low and high-viscosity runs, respectively. This similarity is to be expected, since mass transfer and donor disruption are governed by tidal forces, which are unchanged between the simulations. During coalescence, the evolution of the variable and high-viscosity runs is similar, except that the accretor becomes about twice as hot. In the low-viscosity run, however, the donor's accretion stream produces a contiguous hot ring around the accretor during coalescence, rather than the string of vortices seen in row 2 of Fig. ??, and perturbs the accretor far less. As a result, no distinct void ever forms, though the remnant core is distorted into a bean shape. Within  $\sim 25$  s of coalescence, the void in the high-viscosity simulation is already fast-disappearing, having a radius less than half of that of the variable-viscosity run.  $t_f = 358$  s and 486 s for the high and low-viscosity runs, respectively, compared to 483 s for the variable one. The similarity of the latter two values is likely because the variable-viscosity run tends toward the same  $\alpha$  and  $\beta$  values as the low-viscosity one in the absence of shocks. At  $\sim 500$  s, the remnant has become axisymmetric in all three codes, but in the high-viscosity run the interior  $\sim 0.8 M_\odot$  of the remnant is also rigidly rotating with  $\Omega = 0.33 \text{ s}^{-1}$ , and features a nearly uniform temperature of  $2 - 2.5 \times 10^8 \text{ K}$ .

As expected, then, the high-viscosity simulation rapidly spins down to axisymmetry while eliminating differential rotation, showing that excess artificial viscosity contributes to the disappearance of the crescent-void configuration. The low-viscosity simulation, on the other hand, primarily shows the importance of increasing  $\alpha$  and  $\beta$  during coalescence in order to properly capture shocks and shearing interactions between donor and accretor.

### 5.1.2. Differences in the Merger Process

The disappearance of the hotspot in GASOLINE could have a number of causes: viscosity, spatial resolution, differences in merger structure at coalescence, and SPH surface tension.

The primary differences between the GASOLINE and AREPO simulations arising from the merger up to coalescence include a much earlier and faster mass transfer phase (which we cannot rule out as being an initial conditions effect), a more disrupted accretor (leading to a more crescent-shaped remnant core) and a more prominent, faster-spinning low-density void near the middle of the remnant.

Differences are to be expected, as the merging process involves steep gradients of both density and temperature, shocks from direct impact accretion and supersonic shear flows mixing with each other, all of which are taxing on hydrodynamic codes. Our GASOLINE simulations have poorer spatial resolution than our AREPO simulations, and therefore should

have a harder time capturing steep gradients, and artificial viscosity, even if adaptive, may be insufficient to properly treat a region containing both shocks and shear flows.

We do not note that our high-resolution GASOLINE remnant better approximates our AREPO results than our low-resolution GASOLINE remnant - the remnant core's shape is quite similar at either resolution, both being denser and less crescent-shaped than the core in either AREPO simulation. We did not perform a GASOLINE simulation at comparable spatial resolution to our AREPO simulations to the computational demand of such a simulation.

As an additional check of AREPO's veracity, we ported AREPO's initial conditions to the Eulerian grid code FLASH operating with a fixed grid that has higher resolution close to the remnant core. The post-coalescence evolution in FLASH initially qualitatively resembled that of AREPO, but angular momentum transport was much slower. After XXX s, the transport damped away. If we freeze AREPO's mesh-generating points in space (reducing AREPO to a second-order Eulerian code on an irregular grid), we find a strikingly similar remnant evolution. A close examination of the remnant core's shape shows that, in both FLASH and static-grid AREPO, instead of evolving from a crescent-shaped object into a bar, before becoming spherical, the void simply shrinks over XXX s, as if the crescent's structure was being smeared out. This is consistent with the increased diffusivity of fixed grid codes compared to moving mesh, and similar to the effect of artificial viscosity on the remnant core in GASOLINE, making moving mesh AREPO the only set of simulations that does not artificially smear the core into axisymmetry.

In both GASOLINE and in AREPO the void has a lower pressure than its surroundings, even when including rotational support, but the accretor material around it has high specific angular momentum, which needs to be transported away before the accretor can fill the void.

## 5.2. Post-Merger Evolution and Spurious Angular Momentum Losses

Spiral waves have long been cited as a means for transporting angular momentum in accretion disks (Balbus 2003 and references therein), in particular to accrete material from a disk onto a star or compact object (eg. Sawada et al. 1986, Savonije et al. 1994) and facilitate the inward migration of terrestrial planets (eg. Kley & Nelson 2012). Past simulations have shown that, similar to our case, SPH tends to suppress the expected formation of spiral waves.

de Val-Borro et al. (2006) performed an extensive battery of tests on 17 independent codes, 15 Eulerian and 2 SPH, simulating in two dimensions a planet on a circular orbit interacting with a protoplanetary disk. The planet is expected to tidally excite a spiral wave from each of its two Lindblad resonances and open a density gap in the disk. The Eulerian codes all reproduced these broad features as well as a number of non-linear ones such as vortices at the, and their azimuthal and radial density profiles broadly agreed in shape - in many cases they numerically agree to within a few percent **check with pavel?**. The SPH codes, on the other hand, produce gaps with poorly resolved boundaries (or in the case of shallow gaps, a poorly resolved gap in its entirety) and highly diminished spiral waves. SPH density profile had both different shapes and substantial systematic offsets. Consequently, the tidal torques between the spiral waves and the planet measured by the Eulerian codes was far stronger than the torques measured by the SPH codes. de Val-Borro

et al. (2006) speculated these differences were due to the diffusive nature of SPH, as well as code features like the Balsara switch designed to reduce viscosity in shear flows also leading to poor shock capture in those same regions.

Artificial viscosity has long been cited as hindering the formation of spiral shocks under conditions theoretically favourable to their production (ex. Yukawa et al. 1997; Lanzafame & Belvedere 1997; Lanzafame 2003). In particular, spiral waves more readily develop in 2D disk simulations than in 3D due to the reduced effect of artificial viscosity in 2D (Lanzafame 2003). Lanzafame (2010) attempts a more physically realistic implementations of artificial viscosity, and find stronger spiral waves develop in accretion disks as a result.

Moreover, the remnant core's peanut structure and its surroundings are in no way rigidly rotating, and a strong artificial viscosity quickly drives the remnant toward axisymmetry. An axisymmetric core cannot drive waves through either tides or ram pressure, so artificially smearing out peanut also suppresses angular momentum transport. We find that the  $\alpha = 1$ ,  $\beta = 2$  fixed viscosity GASOLINE test run has the core reach axisymmetry at around XXX s after coalescence,  $\sim 50$  s faster than our production run and XXX s faster than our  $\alpha = 0.05$ ,  $\beta = 0.1$  fixed viscosity test. Artificial viscosity therefore damps both the driving and transport of waves.

In Fig. ?? we again plot the inner angular momentum, this time for our low and high-resolution AREPO simulations, and also plot ones with the same low and high-resolution initial conditions, but without the explicit refinement criterion. Also plotted, in dashed lines, are the total angular momenta of the four simulations over time, shifted downward vertically by  $1.5 \times 10^{10}$  g cm s<sup>-1</sup> to directly compare with inner angular momentum losses. Due to our refinement criteria, all of our AREPO simulations, including those without the explicit criterion, increase in resolution over time. To compare the different simulations, we use  $\langle N \rangle$  the number of mesh-generating points time-averaged over the entire duration of a simulation. Our high resolution simulation has  $\langle N \rangle = XXX$ , our low resolution  $\langle N \rangle = XXX$ , our high resolution simulation without explicit refinement has  $\langle N \rangle = XXX$ , and low resolution without explicit refinement  $\langle N \rangle = XXX$ .

Higher resolution simulations spin down more slowly than their low resolution counterparts, and the spin down ends when the core has more angular momentum remaining. The loss curves for all of these simulations is very similar except for the high-resolution production run. All simulations pass through the same qualitative stages of the spin-down – single spiral wave from a crescent-shaped object transforming to two waves generated by a bar – except the other three simulations experience a smoother evolution from crescent to bar, with no temporary loss in spiral wave strength, than high-resolution production run (Sec. ??). On the other hand, spurious angular momentum losses are reduced almost by a factor of three when going from lowest to highest resolution.

Fig. ?? shows the relationship between time-averaged resolution and fraction of total angular momentum at  $t_{50\%}$ , the time when  $L_{z,\text{tot}} < 9$  has been reduced to 50% its maximum value ( $t_{50\%}$  is larger for higher-resolution simulations because they have slower spin-down). A logarithmic best fit is also plotted, and has the functional form

$$\frac{\Delta L_{z,\text{tot}}}{L_{z,\text{tot}}(t=0)} = -0.034 \langle N \rangle + 0.684 \quad (15)$$

This indicates an extremely slow convergence –

$\Delta L_{z,\text{tot}}/L_{z,\text{tot}}(t=0)$  reduces to below 0.01 only when  $\langle N \rangle > 3 \times 10^8$ . Fig. ?? also shows that having an explicit refinement criterion like we did is important in reducing spurious angular momentum losses, but only because it dramatically increases the total resolution of the simulation. Utilizing extremely high resolutions in our initial conditions, or artificially increasing the resolution after coalescence, would likely produce similar results (though perhaps requiring more computational resources).

To better pinpoint where in the system the angular momentum is being spuriously lost, we performed a calculation, similar to Ji et al. (2013) Sec. 2.2.4, to determine the amount of theoretically expected angular momentum transport. If a fluid is inviscid, then from Euler's Equation the conservation of angular momentum is

$$\frac{\partial L_i}{\partial t} = - \oint_V \epsilon_{ijk} \rho x^j u^k u_l dl^l + \int_V \epsilon_{ijk} x^j F^k dV - \int_V \epsilon_{ijk} x^j \partial^k P dV \quad (16)$$

where the first term is advective, the second external torque and the third pressure torque. We use this equation to calculate the theoretical inner angular momentum  $L_{z,\text{tot}} < 9$  as a function of time, and find the discrepancy between the theoretical and simulation  $L_{z,\text{tot}} < 9$  is greater than 80% of the total spurious angular momentum loss for all our simulations. By the time  $t_{50\%}$  is reached, about two-thirds of  $L_{z,\text{tot}} < 9$  was lost spuriously in the low-resolution simulation without explicit refinement, and  $\sim 35\%$  of  $L_{z,\text{tot}} < 9$  is spuriously lost for our high-resolution, explicitly refined simulation. Just inside  $10^9$  cm is the interface between the high density core and surrounding envelope features, which features large density gradients and shearing, vortices, and other complex fluid flows. These features may be why our simulations, including the GASOLINE 503 s snapshot transplanted into AREPO mentioned in the previous section, are prone to lose angular momentum here instead of in the core and outer disk, which have much more regular bulk motion. This may also be why spurious angular momentum losses are negligible before coalescence, as the core-envelope interface has not yet formed.

We cannot truly make spurious angular momentum losses negligible without going to prohibitively costly resolutions, and they affect all our simulations. At the same time, spiral waves are physically expected due to the non-axisymmetry of the remnant just after coalescence, and from our theoretical angular momentum calculations, comprise the majority of the angular momentum loss observed in the simulation. Our merger remnants all spin down to near-axisymmetry with one, then two, spiral waves regardless of resolution. We therefore believe that the qualitative features of post-merger evolution are robust, while the timescale and exact amount of angular momentum left following spin-down being resolution-sensitive.

Angular momentum conservation issues were not reported in other AREPO and SPH code comparisons, notably among them the large-scale structure formation simulations of Vogelsberger et al. (2012) and galaxy mergers of Hayward et al. (2014), both of which develop disk structures. Hayward et al. (2014) only simulate isolated disk galaxies for a few dozen dynamical times, an order of magnitude less than in our simulations, and then simulate their merger over several dozen additional dynamical times with star formation and supernovae feedback included. Vogelsberger et al. (2012) performs simulations spanning hundreds of dynamical times, but their sim-

ulations feature radiative cooling, a time-dependent ionizing UV background and stellar evolution embedded within an expanding FLRW universe. Both codes have long-range forces dominated by dark matter. Due to these fundamental differences in dynamical times simulated and physics included, we cannot conclude whether the lack of global angular momentum conservation also affects these other works.

**Ruediger, I think we should mention a few other Arepo-only simulations here (Federico's stuff?), and why they don't necessarily suffer from spurious angular momentum losses. What do you think?**

### 5.3. Ramifications for Merger Outcomes

Our current studies somewhat affect the conclusions made for pre-coalescence merger evolution made in other works. A number of previous works (DAN, RASKIN, RUEDIGER?) use relatively low-resolution SPH simulations to try to discern if helium or carbon will violently ignite during the early stages of mass transfer. As we find higher temperatures in newly accreted material during this phase of the merger, we believe that SPH may underestimate the potential for violent nuclear reactions. This has been long-suspected, and is the reason why Guillochon et al. (2010) used a hybrid approach to simulate early mass transfer during a merger. As shown in Fig. ??, the bulk properties and overall profiles between AREPO and GASOLINE are similar, except for the low-density void near the remnant core centre and a much lower core temperature. We performed a number of low-resolution diagnostic tests which show that, even for an unsynchronized, nearly equal-mass 0.625 - 0.626  $M_{\odot}$  merger, the merger remnant remains centrally cold, surrounded by a warmer envelope, in contrast to our SPH results in Zhu et al., as well as Lorén-Aguilar et al..

The more impactful change to the conclusion of other works we make is that hydrodynamic evolution does not stop at coalescence, and a spiral wave-mediated spin down of the merger remnant occurs over several thousand seconds. This spin-down originates from the non-axisymmetry of the remnant core, which itself originates from material from the tidally destroyed donor impacting the accretor. Merger remnants of dissimilar-mass mergers will experience far less accretor disruption than the system we present here, but we find for a low-resolution 0.5 - 1.0  $M_{\odot}$  CO WD merger that the donor does not disrupt into a completely axisymmetric disk around the accretor, and this non-axisymmetry powers a spiral wave propagating into the disk. Hydrodynamic spin down is therefore likely prevalent throughout the majority of the WD merger parameter space.

Because previous works found hydrodynamic evolution to stop at coalescence, it was expected that the next phase of evolution for the remnant would be a magnetically-driven spin-down phase lasting of order hours to days (van Kerkwijk et al. 2010; Shen et al. 2012). Schwab et al. (2012) and Ji et al. (2013) have both simulated this evolution by porting SPH merger results into 2.5D hydrodynamic simulations. Schwab et al. use ZEUS-MP2 fitted with the Helmholtz EoS, a ? shear viscosity set to  $\alpha = 3 \times 10^{-2}$  and a five-isotope nuclear network in order to evolve merger remnants imported from Dan et al. (2011) with a span of masses and compositions. For their fiducial 0.6 - 0.9  $M_{\odot}$  remnant, they find it nearly completely spins down over  $3 \times 10^4$  s, transferring its disk mass and most of its angular momentum into a thermally supported thin envelope (the remnant core barely changes in mass). The material at interface between core and disk, where there is a

temperature peak, is compressed by loss of rotational support such that its temperature increases from  $5 \times 10^8$  K to  $7.5 \times 10^8$  K, and its density from  $2 \times 10^5$  g cm $^{-3}$  to  $6 \times 10^5$  g cm $^{-3}$ . Very little mass is lost. Ji et al. use FLASH in AMR mode to simulate the full magnetohydrodynamic evolution of a 0.6 - 0.6  $M_{\odot}$  remnant ported from Lorén-Aguilar et al. and augmented with a weak poloidal seed magnetic field. Over  $2 \times 10^4$  s, the remnant core loses 70% of its angular momentum, the magnetic field strengthens from  $3 \times 10^5$  G to  $2 \times 10^8$  G, most of the disk mass is accreted onto the remnant (with  $0.06 M_{\odot}$  forming a thin envelope at large distance). The core's central density and temperature rise from  $\sim 2 \times 10^6$  g cm $^{-3}$  and  $\sim 4 \times 10^8$  K to  $\sim 5 \times 10^6$  g cm $^{-3}$  and  $\sim 9 \times 10^8$  K, leading to a core nuclear runaway.

In addition to being more than an order-of-magnitude faster, our hydrodynamic spin-down phase results in a somewhat different remnant. All three simulations agree that disk material will spread outward from the disk plane, and that much of the disk will turn into a thermally-supported hot envelope. The core-envelope interface, which is the location of the off-centre temperature peak, increases in density and temperature from , and the center of the remnant also compresses by a factor of 3. On the other hand, while Ji et al. find their "white dwarf merger" (roughly equivalent to our merger core and dense portion of the thermal envelope g cm $^{-3}$ ) accretes  $0.16 M_{\odot}$ , and Schwab et al. find theirs remains at approximately  $1 M_{\odot}$  (their Fig. 4), our AREPO "WD merger" actually loses mass, from  $1.1 M_{\odot}$  to  $0.95 M_{\odot}$  (and of this, only  $0.65 M_{\odot}$  is degeneracy energy dominated; see Fig. ??). We also find no unbound outflow of mass, even though our mass resolution,  $10^{-6} M_{\odot}$  is three orders of magnitude below the mass loss reported by Ji et al. and one below that reported by Schwab et al.. That Ji et al. (2013) find a central nuclear runaway, and we do not, is primarily due to their use of Lorén-Aguilar et al. (2009)'s 0.6 - 0.6  $M_{\odot}$  remnant, than differences in post-coalescence evolution. At Lorén-Aguilar et al.'s remnant has its highest temperature at the center of the core, and is overall much hotter than our AREPO (and even our GASOLINE) remnant just after coalescence.

With most of the rotational energy in the entire system converted to thermal energy, viscous evolution will be unimportant to the spun-down remnant. As discussed in Shen et al. (2012), thermal evolution will now dominate the system. Throughout much of the envelope, radiation pressure is comparable or exceeds gas pressure, and so the remnant's luminosity will be of order the Eddington luminosity (Shen et al. 2012), and may also launch a wind. Our spun-down remnant contains a shell of  $\sim 10^6$  g cm $^{-3}$  material at  $\sim 8 \times 10^7$  K, which is sufficient to generate a convective carbon burning shell. The end state of this evolution is likely an oxygen-neon WD (Nomoto & Iben 1985; Shen et al. 2012). Since the total system mass is far below the Chandrasekhar mass, the densities required for accretion-induced collapse will not be reached. While we substitute a viscous angular momentum transport phase for a hydrodynamic one, we do not predict, based on the results in this paper, the final outcome of a merger to be all that different from previous expectations.

## 6. CONCLUSIONS

We perform a comparison between a simulation of a 0.625 - 0.65  $M_{\odot}$  merger performed in SPH GASOLINE with one performed in AREPO moving mesh. We find higher temperatures for newly accreted material before coalescence, and a more

well-defined hot, low density void, as well as a greater temperature contrast between the void and dense remnant core material, just following coalescence. We believe these differences to be due to SPH's artificial viscosity in concert with poorer shock and instability capturing. Following coalescence, the merger remnant in AREPO begins a phase of rapid angular momentum transport mediated by spiral waves that are launched from the remnant core into the surrounding medium. These waves cause the remnant core to lose most of its angular momentum and achieve near-spherical symmetry. As SPH is known to suppress spiral waves and other disk structures, we believe the earliest phase of post-merger evolution is more accurately captured in AREPO.

While we do find novel hydrodynamic behaviour in our AREPO simulations we believe are being artificially suppressed in SPH simulations, we also found unphysical angular momentum losses in AREPO that were only discovered through our comparative analysis, and future simulations must still be performed with caution. Despite its shortcomings, SPH still appears superior in maintaining conserved quantities over hundreds of dynamical times. It remains to be seen if novel formulations of SPH can once again make it the preferred choice for simulating mergers.

Moreover, our simulation were more test cases than accurate representations of mergers: missing are nuclear reactions, possible synchronization (Fuller & Lai 2012; Burkart et al. 2013), proper modelling of the tidal bulges (for either synchronized or unsynchronized binaries) and other essential features of a complete picture of white dwarf mergers. In particular, the generation of a strong global magnetic field out of a dynamically negligible seed field would likely occur in a merger, since **EVIDENCE FROM SINGLE WDs AND NON-MERGING BINARIES**. We believe this hetherto neglected aspects of mergers to be of prime importance to the dynamics of mergers, and are currently exploring its effects using AREPO MHD simulations.

We thank Volker Springel, James Wadsley, Christopher Matzner, Ue-Li Pen and Stephen Ro for their insight into hydrodynamics and simulations. This work was supported by the Natural Sciences and Engineering Research Council (NSERC) Vanier Canada Graduate Scholarship and Reinhardt Endowment Travel Fund. Computations were performed on the GPC supercomputer at the SciNet HPC Consortium. SciNet (Loken et al. 2010) is funded by the Canada Foundation for Innovation under the auspices of Compute Canada, the Government of Ontario, Ontario Research Fund - Research Excellence and the University of Toronto.

## REFERENCES

- Agertz, O. et al. 2007, MNRAS, 380, 963  
 Balbus, S. A. 2003, ARA&A, 41, 555  
 Balsara, D. S. 1995, Journal of Computational Physics, 121, 357  
 Benz, W., Cameron, A. G. W., Press, W. H., & Bowers, R. L. 1990, ApJ, 348, 647  
 Burkart, J., Quataert, E., Arras, P., & Weinberg, N. N. 2013, MNRAS, 433, 332  
 Cha, S.-H. & Wood, M. A. 2016, MNRAS, 458, 480  
 Dan, M., Rosswog, S., Brüggen, M., & Podsiadlowski, P. 2014, MNRAS, 438, 14  
 Dan, M., Rosswog, S., Guillochon, J., & Ramirez-Ruiz, E. 2011, ApJ, 737, 89  
 —. 2012, MNRAS, 422, 2417  
 de Val-Borro, M. et al. 2006, MNRAS, 370, 529  
 Dehnen, W. & Aly, H. 2012, MNRAS, 425, 1068  
 Dolag, K., Vazza, F., Brunetti, G., & Tormen, G. 2005, MNRAS, 364, 753  
 Duffell, P. C. & MacFadyen, A. I. 2011, ApJS, 197, 15  
 Eggleton, P. P. 1983, ApJ, 268, 368  
 Feiden, G. A. & Chaboyer, B. 2012, ApJ, 761, 30  
 Fryxell, B. et al. 2000, ApJS, 131, 273  
 Fuller, J. & Lai, D. 2012, MNRAS, 421, 426  
 Gaburov, E., Johansen, A., & Levin, Y. 2012, ApJ, 758, 103  
 Goedbloed, J. P. H. & Poedts, S. 2004, Principles of Magnetohydrodynamics  
 Governato, F. et al. 2015, MNRAS, 448, 792  
 Guerrero, J., García-Berro, E., & Isern, J. 2004, A&A, 413, 257  
 Guillochon, J., Dan, M., Ramirez-Ruiz, E., & Rosswog, S. 2010, ApJ, 709, L64  
 Hayward, C. C., Torrey, P., Springel, V., Hernquist, L., & Vogelsberger, M. 2014, MNRAS, 442, 1992  
 Hernquist, L. & Katz, N. 1989, ApJS, 70, 419  
 Hopkins, P. F. 2013, MNRAS, 428, 2840  
 Hu, C.-Y., Naab, T., Walch, S., Moster, B. P., & Oser, L. 2014, MNRAS, 443, 1173  
 Ji, S. et al. 2013, ApJ, 773, 136  
 Katz, M. P., Zingale, M., Calder, A. C., Swesty, F. D., Almgren, A. S., & Zhang, W. 2016, ApJ, 819, 94  
 Keller, B. W., Wadsley, J., Benincasa, S. M., & Couchman, H. M. P. 2014, MNRAS, 442, 3013  
 Keller, B. W., Wadsley, J., & Couchman, H. M. P. 2015, MNRAS, 453, 3499  
 Kleinman, S. J. et al. 2013, ApJS, 204, 5  
 Kley, W. & Nelson, R. P. 2012, ARA&A, 50, 211  
 Lanzaflame, G. 2003, A&A, 403, 593  
 —. 2010, MNRAS, 408, 2336  
 Lanzaflame, G. & Belvedere, G. 1997, MNRAS, 284, 957  
 Loken, C. et al. 2010, Journal of Physics Conference Series, 256, 012026  
 Lorén-Aguilar, P., Isern, J., & García-Berro, E. 2009, A&A, 500, 1193  
 Maeder, A., Meynet, G., Lagarde, N., & Charbonnel, C. 2013, A&A, 553, A1  
 Marinacci, F., Pakmor, R., & Springel, V. 2014, MNRAS, 437, 1750  
 Mitchell, N. L., McCarthy, I. G., Bower, R. G., Theuns, T., & Crain, R. A. 2009, MNRAS, 395, 180  
 Miyoshi, T. & Kusano, K. 2005, Journal of Computational Physics, 208, 315  
 Moll, R., Raskin, C., Kasen, D., & Woosley, S. E. 2014, ApJ, 785, 105  
 Monaghan, J. J. 2005, Reports on Progress in Physics, 68, 1703  
 Nomoto, K. & Iben, Jr., I. 1985, ApJ, 297, 531  
 Ohlmann, S. T., Röpke, F. K., Pakmor, R., & Springel, V. 2016, ApJ, 816, L9  
 Pakmor, R., Bauer, A., & Springel, V. 2011, MNRAS, 418, 1392  
 Pakmor, R., Kromer, M., Röpke, F. K., Sim, S. A., Ruiter, A. J., & Hillebrandt, W. 2010, Nature, 463, 61  
 Pakmor, R., Kromer, M., Taubenberger, S., Sim, S. A., Röpke, F. K., & Hillebrandt, W. 2012, ApJ, 747, L10  
 Pakmor, R., Kromer, M., Taubenberger, S., & Springel, V. 2013, ApJ, 770, L8  
 Pakmor, R. & Springel, V. 2013, MNRAS, 432, 176  
 Pakmor, R. et al. 2016, MNRAS, 455, 1134  
 Papaloizou, J. C. B. & Lin, D. N. C. 1995, ARA&A, 33, 505  
 Raskin, C., Kasen, D., Moll, R., Schwab, J., & Woosley, S. 2014, ApJ, 788, 75  
 Raskin, C., Scannapieco, E., Fryer, C., Rockefeller, G., & Timmes, F. X. 2012, ApJ, 746, 62  
 Savonje, G. J., Papaloizou, J. C. B., & Lin, D. N. C. 1994, MNRAS, 268, 13  
 Sawada, K., Matsuda, T., & Hachisu, I. 1986, MNRAS, 219, 75  
 Schwab, J., Shen, K. J., Quataert, E., Dan, M., & Rosswog, S. 2012, MNRAS, 427, 190  
 Segretain, L., Chabrier, G., & Mochkovitch, R. 1997, ApJ, 481, 355  
 Shen, K. J., Bildsten, L., Kasen, D., & Quataert, E. 2012, ApJ, 748, 35  
 Shen, S., Wadsley, J., & Stinson, G. 2010, MNRAS, 407, 1581  
 Springel, V. 2005, MNRAS, 364, 1105  
 —. 2010a, MNRAS, 401, 791  
 —. 2010b, ARA&A, 48, 391  
 Tamburello, V., Mayer, L., Shen, S., & Wadsley, J. 2015, MNRAS, 453, 2490  
 Timmes, F. X. & Swesty, F. D. 2000, ApJS, 126, 501  
 Trac, H., Sills, A., & Pen, U.-L. 2007, MNRAS, 377, 997  
 Tremblay, P.-E. & Bergeron, P. 2009, ApJ, 696, 1755  
 van Kerkwijk, M. H., Chang, P., & Justham, S. 2010, ApJ, 722, L157  
 Vandenbroucke, B. & De Rijcke, S. 2016, Astronomy and Computing, 16, 109  
 Vogelsberger, M., Sijacki, D., Kereš, D., Springel, V., & Hernquist, L. 2012, MNRAS, 425, 3024  
 Wadsley, J. W., Stadel, J., & Quinn, T. 2004, New Astr., 9, 137  
 Yukawa, H., Boffin, H. M. J., & Matsuda, T. 1997, MNRAS, 292, 321  
 Zhu, C., Chang, P., van Kerkwijk, M. H., & Wadsley, J. 2013, ApJ, 767, 164

Zhu, C., Pakmor, R., van Kerkwijk, M. H., & Chang, P. 2015, ApJ, 806, L1